ADVANCED OPTICAL MATERIALS
www.advopticalmat.de

Hybrid Perovskite Degradation from an Optical Perspective: A Spectroscopic Ellipsometry Study from the Deep Ultraviolet to the Middle Infrared

Alvaro Tejada, Sven Peters, Amran Al-Ashouri, Silver Hamill Turren-Cruz, Antonio Abate, Steve Albrecht, Florian Ruske, Bernd Rech, Jorge Andrés Guerra,* and Lars Korte**

AbstractA quantitative analysis of the thermally induced degradation of various device-relevant multi-cation hybrid perovskite films is performed using spectroscopic ellipsometry, for temperatures between 80 and 120 °C. The studied compositions are a triple cation perovskite $Cs_{0.05}(MA_{0.17}FA_{0.83})_{0.95}Pb(Br_{0.17}I_{0.83})_3$, a Rb-containing variant $Rb_{0.05}Cs_{0.05}(MA_{0.17}FA_{0.83})_{0.90}Pb(Br_{0.17}I_{0.83})_3$, and a methylammonium-free $Rb_{0.05}Cs_{0.10}FA_{0.85}PbI_3$ composition. A very wide combined spectral range of 200 nm to 25 µm is covered by combining the data from two separate instruments. The relative changes in organic cation concentrations are quantified from the middle infrared molecular absorption bands, leveraging the use of point-by-point fitting for increased sensitivity. Additionally, the formation of PbI_2 and non-perovskite δ-$CsPbI_3$ phases is evidenced from Bruggemann effective medium fits to the visible and ultraviolet complex refractive indices. Methylammonium is almost completely depleted from the relevant compositions within 100 to 285 min of thermal annealing. The MA-free perovskite degrades faster at intermediate temperatures, which is attributed to phase instability due to the formation of δ-$CsPbI_3$ in addition to PbI_2.

1. Introduction

Organic–inorganic hybrid perovskites are a promising class of absorber materials for upcoming generations of high-efficiency thin film solar cells.[1–15] This is due to a combination of excellent semiconductor properties, including a direct and tunable bandgap, a sharp absorption edge,[1,7,8] and low recombination losses,[9] with a compatibility for deposition by low-cost solution processing methods. This potential has been evidenced by the current power conversion efficiency records of 25.5%[12] for single junction perovskite solar cells, and 29.5% for dual junction silicon/perovskite tandem cells.[16]

So far, the main limitation of such devices has been the low stability of perovskites under the influence of environmental factors, such as UV irradiation,[3,4,13–15,17–22] moisture,[3,4,15,17,22] or high ambient and/or process temperatures.[3,9,10,14,15,17–19,22] This issue has been greatly mitigated through compositional engineering, which has yielded several promising perovskite recipes using combinations of methylammonium (MA) and formamidinium (FA) organic cations.[2–4,9,10] This work thus sets out to characterize the compositional and structural changes of various device-relevant perovskites, under the effects of high temperatures, through spectroscopic ellipsometry.

A. Tejada, A. Al-Ashouri, S. Albrecht, F. Ruske, L. Korte
Helmholtz-Zentrum Berlin für Materialien und Energie GmbH
Young Investigator Group for Perovskite Tandem Solar Cells
Kekuléstraße 5, 12489 Berlin, Germany
E-mail: korte@helmholtz-berlin.de

A. Tejada, J. A. Guerra
Departamento de Ciencias
Sección Física
Pontificia Universidad Católica del Perú
Av. Universitaria 1801, Lima 15088, Peru
E-mail: atejadae@pucp.edu.pe; guerra.jorgea@pucp.edu.pe

The ORCID identification number(s) for the author(s) of this article can be found under https://doi.org/10.1002/adom.202101553.

DOI: 10.1002/adom.202101553

S. Peters
SENTECH Instruments GmbH
Schwarzschildstraße 2, 12489 Berlin, Germany

S. H. Turren-Cruz, A. Abate
Helmholtz-Zentrum Berlin für Materialien und Energie GmbH
Department Novel Materials and interfaces for photovoltaic solar cells
Kekuléstraße 5, 12489 Berlin, Germany

B. Rech
Helmholtz-Zentrum Berlin für Materialien und Energie GmbH
Scientific Management
Hahn-Meitner-Platz 1, 14109 Berlin, Germany

Spectroscopic ellipsometry has been used widely for the characterization of perovskites,[1,7,8,23–26] including studies on the effects of thermally induced degradation.[17,27] Expanding on these works, this study employs a very wide spectral range, spanning from the deep ultraviolet (DUV) to the middle infrared (MIR). In this way, changes in the concentration of the organic cations can be inferred from their vibrational absorption bands in the MIR, while the formation of PbI_2 and non-perovskite δ-$CsPbI_3$ as degradation by-products was modeled from their effects in the DUV to near infrared (NIR). We believe the outlined methodologies will be useful to those working with hybrid perovskites, as they require only quick and non-destructive measurements,[25,28] and allow quantitative analyses of both chemical and structural properties. As these methodologies can also be applied to more complex film arrangements, we believe they will also be relevant to those working on perovskite solar cells, since the aforementioned processes also take place in fully assembled perovskite devices.[14] Note that, in devices, additional degradation mechanisms are also present.[13]

Three different device-relevant perovskites were studied. First is a “triple cation” perovskite composition $Cs_{0.05}(MA_{0.17}FA_{0.83})_{0.95}Pb(Br_{0.17}I_{0.83})_3$, which is known for its high stability and efficiency in solar cells,[3,5,9] and has been successfully implemented in silicon/perovskite tandem cells.[2] Two Rb-containing compositions were also considered, as these have shown further improved thermal stability.[4,9,10] One is a “quadruple cation” $Rb_{0.05}Cs_{0.05}(MA_{0.17}FA_{0.83})_{0.90}Pb(Br_{0.17}I_{0.83})_3$ composition[9] similar to the aforementioned. The other is a MA-free $Rb_{0.05}Cs_{0.10}FA_{0.85}PbI_3$ composition.[10] The latter was chosen due the MA cation’s tendency to decompose and/or escape the film, which is considered to be one of the weakest links in the durability of hybrid perovskites.[10,17,20,22,29]

2. Methodology

2.1. Sample Preparation

For all perovskite samples, 2.5×2.5 cm^2 silicon substrates coated with ITO and a hole transporting material (HTM) were used. This particular substrate stack was chosen in order to replicate as closely as possible the growth conditions of the perovskite on a silicon/perovskite p-i-n tandem solar cell structure.[2,11] The silicon substrates were cut from lowly doped (1–5 kΩ. cm) n-type single-side polished 400 µm thick (100) float zone wafers. Prior to the ITO deposition, substrates were subjected to an RCA cleaning procedure,[30] followed by a short etching in 1% HF in H_2O to strip any remaining silicon oxide layers. The ITO was grown by DC magnetron sputtering with a substrate temperature of 200 °C in an in-line tool (Leybold Optics A600V7). After UV–ozone cleaning of the substrates, the HTM was deposited atop the ITO in an N_2-purged glovebox. For the triple cation perovskite samples, the HTM consisted of MeO-2PACz self-assembled monolayers (SAMs), which were formed by dip coating.[11,31] For the Rb-containing perovskite samples, the HTM was instead a 10 nm poly[bis(4-phenyl)(2,4,6-trimethylphenyl)amine] (PTAA) layer, deposited by spin-coating.

The perovskite films were deposited shortly after the HTM deposition in a separate N_2-purged glovebox, without intermediate air exposure of the substrates. All perovskite films were deposited by spin coating from stock solutions, which were themselves prepared in another N_2-purged glovebox. The stoichiometries of the final perovskite films were derived from those of the respective stock solutions. The preparation was similar to previously published recipes.[3–5,10] A detailed description of the procedure can be found in the Supporting Information.

2.2. Thermal Degradation Process

All samples were stored in a N_2-purged glovebox prior to the degradation tests, and transported in sealed N_2-filled plastic bags to the experiment site. In this way, samples were not exposed to air, from fabrication up until just before beginning the degradation tests. Samples were degraded by exposure to temperatures of 80, 100, and 120 °C on a hotplate. These temperatures were chosen in consideration of the maximum operating temperatures typically expected for silicon solar cells, those used during testing of perovskite solar cells,[15] as well as those used during the fabrication of the considered perovskite compositions.[2,9,10] The degradation process was carried out within in a glass dome and under N_2 flow to minimize oxygen- and moisture-induced degradation.[22] All samples were periodically removed from the hotplate, allowed to cool to room temperature, measured at the ellipsometers, and subsequently returned to the hotplate for further degradation. This was kept up for total degradation times of 165 to 285 min, depending on the temperature.

2.3. Measurements

Ellipsometry measurements were carried out from the DUV to MIR spectral regions by subsequent measurements on two different ellipsometers with overlapping spectral ranges. The DUV to NIR regions were measured using a Sentech SENResearch 4.0 combined CCD array and FTIR ellipsometer, covering 200 to 2500 nm, with angles of incidence of 55°, 65°, and 75°, and a measurement spot diameter of ≈3 mm. The MIR region was measured with a Sentech SENDIRA FTIR ellipsometer, covering 1.7 to 25 µm (400 to 6000 cm^{-1}), with an angle of incidence of 65°, and a measurement spot diameter of ≈6 mm. The MIR ellipsometer body was purged with N_2 to reduce the parasitic absorbtion by CO_2 and H_2O along the light path. All ellipsometry measurements were performed with the sample in air in a climate controlled room with a temperature of 20 °C and relative humidity below 20%. Each complete set of measurements took approximately 8 min. Degradation of the samples during the ellipsometry measurements was considered negligible. To support this, a set of control samples was kept exposed to the ambient air in the same room during the entire experiment, with no significant changes in their (Ψ, Δ) spectra observed throughout. Care was taken to center the measurement spots onto the same location on each sample in both instruments. Additionally, all (Ψ, Δ) spectra were verified to match in the overlapping spectral regions of both instruments at the angle of incidence of 65°.

Supplementary scanning electron microscope (SEM) images and X-ray diffraction (XRD) measurements of selected samples before and after the degradation tests were also performed. These were obtained, respectively, using a Zeiss Merlin SEM with a Schottky field emission source and in-lens detector, and a Bruker D8 Discover diffractometer in Bragg–Brentano geometry.

2.4. Ellipsometry Fitting

All (Ψ, Δ) spectra were fitted using the SpectraRay/4 software by Sentech. A stack of bulk c-Si/ITO/HTM/ perovskite/surface roughness was assumed for the optical model. In samples using SAMs, the HTM layer was omitted as its impact on the measurement is negligible. This was verified by comparing bare substrates before and after SAM layer coating, in which the overall (Ψ, Δ) spectra show no significant changes. In all cases, surface roughness was modeled using a Bruggemann effective medium approximation (EMA) with 50% voids.

The substrate ITO layer was modeled with a combination of three Tauc–Lorentz oscillators to account for the bandgap and high energy absorption, and a Drude dispersion model for the free carrier absorption. Due to the graded structure commonly observed in ITO, it is convenient to model it as a stack of homogeneous layers with differing free carrier absorption parameters.[32] In this case, due to the low penetration depth at photon energies above the ITO's bandgap, two layers with shared Tauc–Lorentz parameters but differing Drude parameters were sufficient to describe its behavior throughout the combined spectral range. It was unnecessary to consider backside reflections in the c-Si wafer as it was only single-side polished, and due to significant free carrier absorption in the ITO at photon energies below 1 eV.

When applicable, the overlaying PTAA layer was modeled with two Tauc–Lorentz oscillators, yielding (*n*, *k*) spectra similar to reported values.[33] Fits were performed simultaneously to two samples: one of PTAA on the c-Si/ITO stack and one of pure PTAA on fused silica. This was done for improved sensitivity as the PTAA layers are quite thin (≈10 nm) and do not contrast strongly with the ITO. A schematic of the optical model is shown in **Figure 1**, and the (*n*, *k*) spectra for the ITO and PTAA layers can be observed in Figure S1, Supporting Information.

In the MIR region, the perovskite samples were fitted using a three step approach. The (Ψ, Δ) spectra were first fitted using a combination of a constant refractive index for the baseline dispersion and a series of Brendel oscillators for the primary vibrational absorption bands. The fitted film thickness and roughness were then taken as constant and the complex refractive index was solved point-by-point for each individual wavelength, thus providing model-free dispersion data.[1,7,8] By doing so, it was possible to resolve very small peaks and subtle features such as shoulders on the sides of large peaks, which are difficult to distinguish in the (Ψ, Δ) spectra. Finally, the resulting (*n*, *k*) spectra were themselves fitted with a more complete series of Brendel oscillators for a complete description and to ensure Kramers–Kronig consistency.

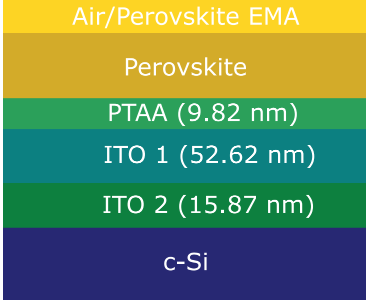

Figure 1. Schematic of the optical model used for ellipsometry fits on the perovskite samples using PTAA.

In the DUV to NIR regions, a combination of two Tauc–Lorentz oscillators for the absorption edge and seven Gaussian oscillators for the higher energy transitions was used. This procedure was chosen in favor of using only Tauc–Lorentz oscillators, as is common,[23] due the lower number of free parameters (one less per oscillator) and therefore quicker convergence of the fits. An example fit is shown in **Figure 2**. Typical film thicknesses were in the range of 400–550 nm. One or two additional Tauc–Lorentz oscillators were considered to account for the formation of PbI_2 and δ-$CsPbI_3$ as the perovskites degraded, with absorption onsets around 2.4[7] and 2.85 eV,[6,27] respectively. These features can be observed in Figure 8.

It is important to consider the effects induced by the pronounced surface roughness typical of solution-processed perovskites. In the MIR fits, typical roughness layer thickness values

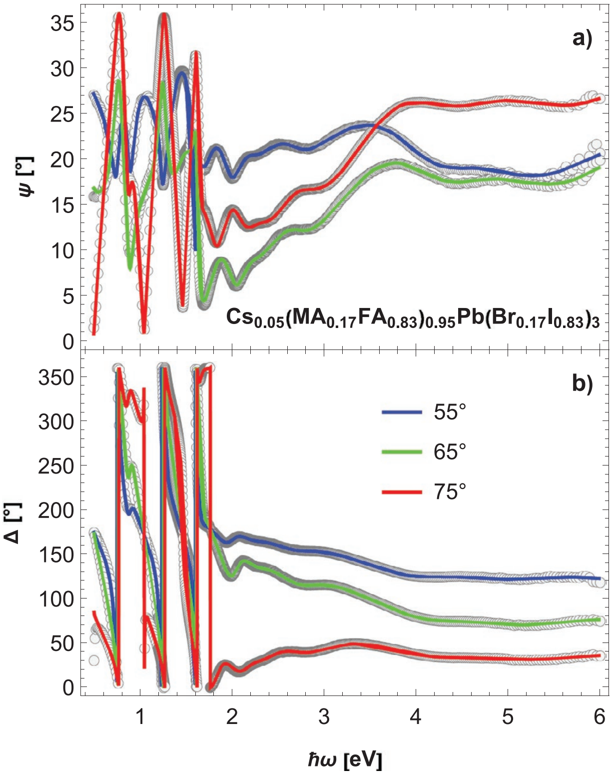

Figure 2. Example of fitted ellipsometry spectra in the DUV to NIR regions. The data correspond to an undegraded $Cs_{0.05}(MA_{0.17}FA_{0.83})_{0.95}Pb(Br_{0.17}I_{0.83})_3$ perovskite sample. For ease of viewing, only one in every three data points is shown.

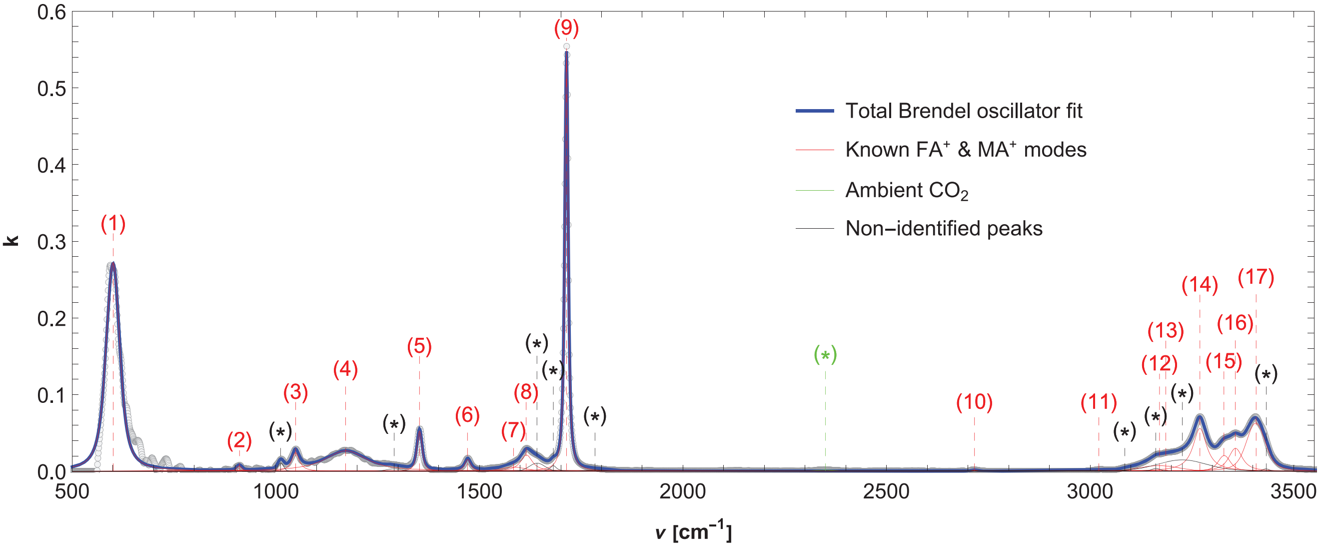

Figure 3. Extinction coefficient *k* for an undegraded triple cation $Cs_{0.05}(MA_{0.17}FA_{0.83})_{0.95}Pb(Br_{0.17}I_{0.83})_3$ perovskite sample in the MIR region. Grey circles correspond to the point-by-point solution. All known vibrational modes attributed to the FA^+ and MA^+ cations are shown and labeled in red, the contribution of ambient CO_2 in green, and all unknown peaks in black. Peak assignments are detailed in Table 1.

were in the range of 20–30 nm, which is consistent with the film topography observed in the SEM images, as can be seen in Figures S2–S4, Supporting Information. However, in the DUV to NIR fits, roughness values were much lower, in the range of 1–6 nm. This discrepancy could be partially due to differences in spot size and/or alignment between the two ellipsometers; however, it is mainly attributed to the known limitations of EMAs, as these are only valid when layer features are much smaller than the probing wavelength (λ). Otherwise, light scattering and depolarization occur, leading to distortions in the fitted (n, k) spectra, sub-bandgap absorption and underestimated fitted roughness. A classic rule of thumb is that EMA layers should be no thicker than 0.1λ.[24,28] Therefore, the film thickness and roughness layer values from the MIR fits are considered more reliable, as probing wavelengths are much larger.

3. Results and Discussion

3.1. Undegraded Perovskites

The extinction coefficient k in the MIR region for an undegraded triple cation perovskite sample is shown in **Figure 3**. Various peaks corresponding mostly to molecular bond vibrational modes within the FA^+ and MA^+ cations can be observed. The assignments of all known peaks[6,34–37] are detailed in **Table 1**. The absorption spectrum is shown in terms of k instead of the absorption coefficient $\alpha = 4\pi k/\lambda$, as is customary, because the volumetric bond density corresponding to each peak is then directly proportional to the peak area,[38] that is, the area of each sub-peak shown in red. This then provides a more balanced visual representation of the concentration of each cation. The spectra for the undegraded Rb-containing perovskites are very similar, except for the $Rb_{0.05}Cs_{0.10}FA_{0.85}PbI_3$ perovskite lacking the peaks associated with MA, as would be expected. The full (n, k) spectra for all undegraded perovskites are shown in Figure S5, Supporting Information. No peaks associated with the HTM layers[31,39] could be distinguished, likely due to their comparatively very low thicknesses.

The (n, k) spectra in the DUV to NIR regions corresponding to undegraded samples of all three perovskite compositions are shown in **Figure 4**. For reference, the dispersion of $MAPbI_3$ obtained point-by-point from combined reflection/transmission and ellipsometry[1] is also shown. In their pristine condition, all compositions show very similar (n, k) spectra. The main differences are the absorption edge positions, due to the slight differ-

Table 1. Assignments to known vibrational modes for MIR peaks shown in Figure 3.

Label	Center [cm⁻¹]	Peak assignment
1	599	FA^+ - C-H rock
2	910	MA^+ - CH_3-NH_3^+ rock
3	1048	FA^+ - C-H stretch
4	1173	FA^+ - C-N stretch
5	1353	FA^+ - C-N stretch
6	1472	MA^+ - sym. NH_3^+ bend
7	1584	MA^+ - asym. NH_3^+ bend
8	1616	FA^+ - N-H bend
9	1713	FA^+ - C=N stretch
10	2716	MA^+ - sym. NH_3^+bend + CH_3-NH_3^+ rock
11	3022	MA^+ - asym. CH_3 stretch
12	3170	FA^+ - N-H stretch
13	3186	MA^+ - asym. NH_3^+ bend
14	3269	FA^+ - C-H stretch
15	3329	FA^+ - N-H bend
16	3357	FA^+ - sym. N-H stretch
17	3407	FA^+ - asym. N-H stretch

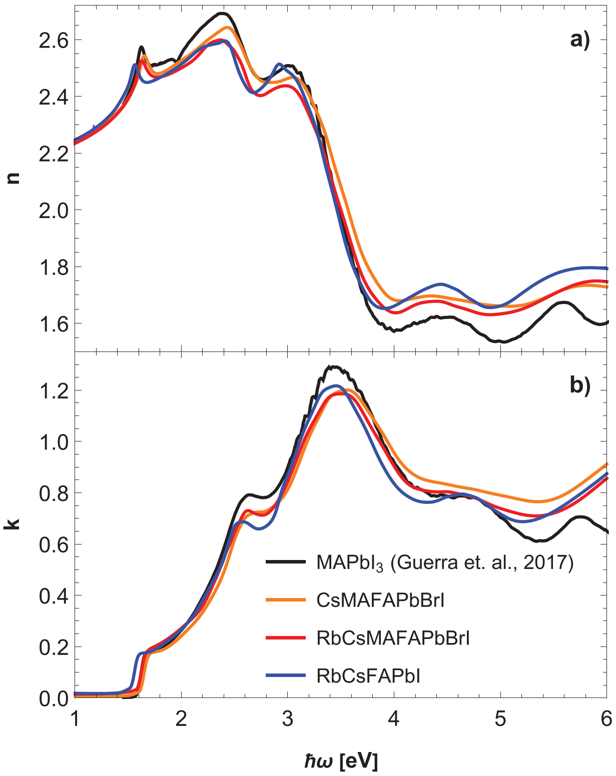

Figure 4. *n* (a) and *k* (b) spectra for undegraded samples of all considered perovskite compositions as well as $MAPbI_3$ in the DUV to NIR regions.

ences in bandgap, and variations in the higher energy (2–6 eV) absorption. Besides compositional differences, the latter are attributed to surface roughness effects, both due to the aforementioned limitations of EMAs, as well as the shallow light penetration depth in this region, resulting in greater uncertainty of the optical constants.

3.2. Degradation Effects in the MIR Region

Upon exposure to high temperatures, all of the considered perovskite compositions show significant changes in their overall (*n*, *k*) spectra. In the MIR region, all peaks attributed to the organic cations change over time, which indicates changes in the corresponding bond densities. At the same time, the baseline refractive index remains mostly constant (see Figure S6, Supporting Information). Considering the Clausius–Mossotti/Lorentz–Lorentz equation, which relates density to the refractive index,[40,41] it can be surmised that the film density does not change significantly. Consequently, any changes in bond density correspond mainly to changes in the cation concentrations, and thus both quantities are proportional to the respective peak areas. The relative changes in the area of these peaks can thus readily be used to quantify the changes in cation concentration.

For methylammonium, only the peak at 1472 cm^{-1} (symmetric NH_3^+ bending) can be used for quantification, as the other peaks corresponding to this cation are far too small to track consistently. The relative changes in the area of this peak over time are shown in **Figure 5**. For reference, error bars corresponding to a fit sensitivity analysis by the SpectraRay/4 software are shown for one dataset. It can be seen that the MA concentration decreases considerably over time, especially at higher temperatures. At 120 °C, the peak at 1472 cm^{-1} becomes undetectable after 105 min for the triple cation perovskite, and after 170 min for the Rb-containing perovskite, suggesting a near total depletion of MA in the films by this point.

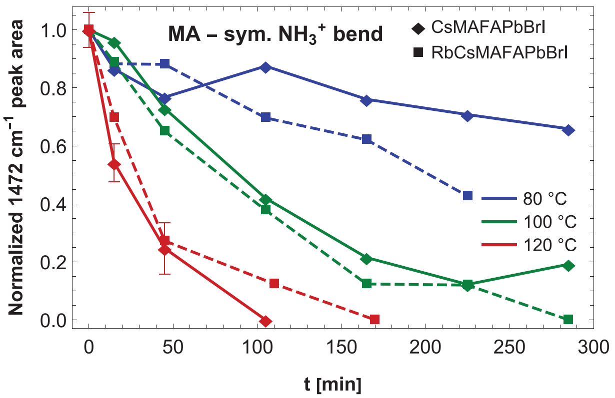

Figure 5. Relative variation during thermally-induced degradation of the area under the 1472 cm^{-1} sub-peak, corresponding to a symmetric NH_3^+ bending mode in methylammonium. Solid lines correspond to the $Cs_{0.05}(MA_{0.17}FA_{0.83})_{0.95}Pb(Br_{0.17}I_{0.83})_3$ composition, while dashed lines correspond to $Rb_{0.05}Cs_{0.05}(MA_{0.17}FA_{0.83})_{0.90}Pb(Br_{0.17}I_{0.83})_3$. Values of zero indicate the peak is undetectable.

To assess the changes in formamidinium concentration, several high intensity peaks are available. It is inconvenient to use peaks in the N-H mode cluster in the 2900–3500 cm^{-1} range, as it would require deconvolving several superimposed peaks, some of which could not be attributed to known modes. At the same time, the peak at 599 cm^{-1} (C-H rocking) is in a region with a lower signal-to-noise ratio, thus limiting precision. Therefore, the highest intensity peak at 1713 cm^{-1} (C=N stretching) was chosen. The relative changes in the area of this peak over time are shown in **Figure 6**. For reference, error bars corresponding to a fit sensitivity analysis by the SpectraRay/4 software are shown for one dataset. For the MA-containing perovskites (Figure 6 a,b), the FA concentration initially increases over time, in tandem with the decrease in MA concentration (Figure 5), and then decreases as MA is depleted. This behavior is more pronounced at higher temperatures, although the scale of the variations is much smaller than for MA. For the MA-free perovskite, the FA concentration drops monotonously, curiously with a slightly greater loss at 100 °C than at 120 or 80 °C. Further insight into this behavior is provided at the end of Section 3.3.

The initial increase in FA concentration for the MA-containing perovskites may seem counterintuitive, but it is a natural consequence of the change in film stoichiometry during degradation. Both MA and FA constitute considerable fractions of the film bulk. If MA is then lost at much higher rates than FA for the same given sample and temperature, then initially an appreciable amount of material will be lost from the films as the MA content is depleted. The film density does not change significantly; therefore, the films shrink while the total amount of FA varies only slightly. This results in a higher concentration of FA cations, and thus larger areas under the 1713 cm^{-1} peak.

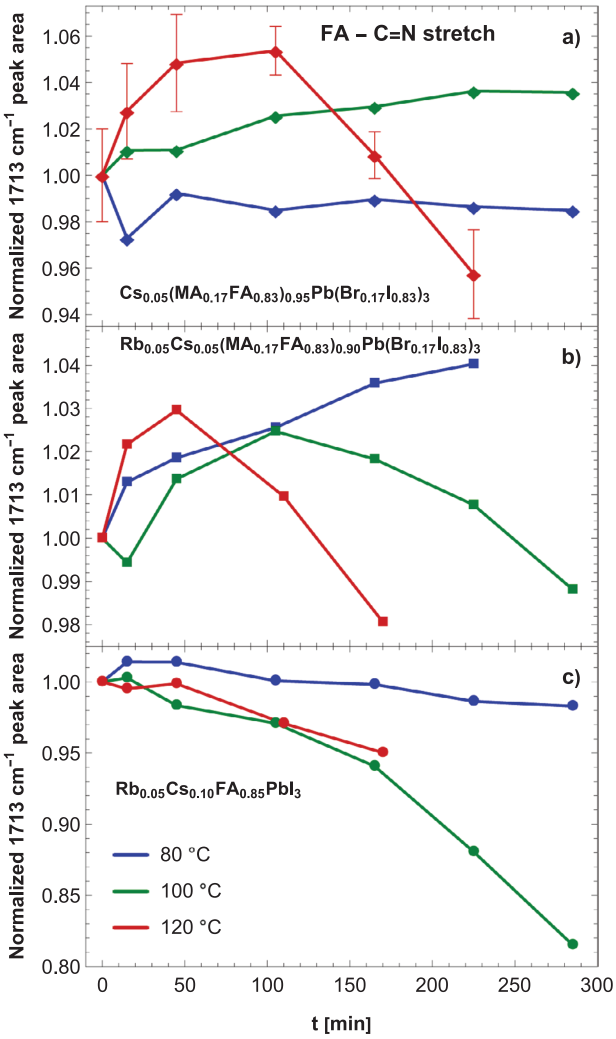

Figure 6. Relative variation during thermally induced degradation of the area under the 1713 cm^{-1} sub-peak, corresponding to a C=N stretching mode in formamidinium, for all considered perovskite compositions.

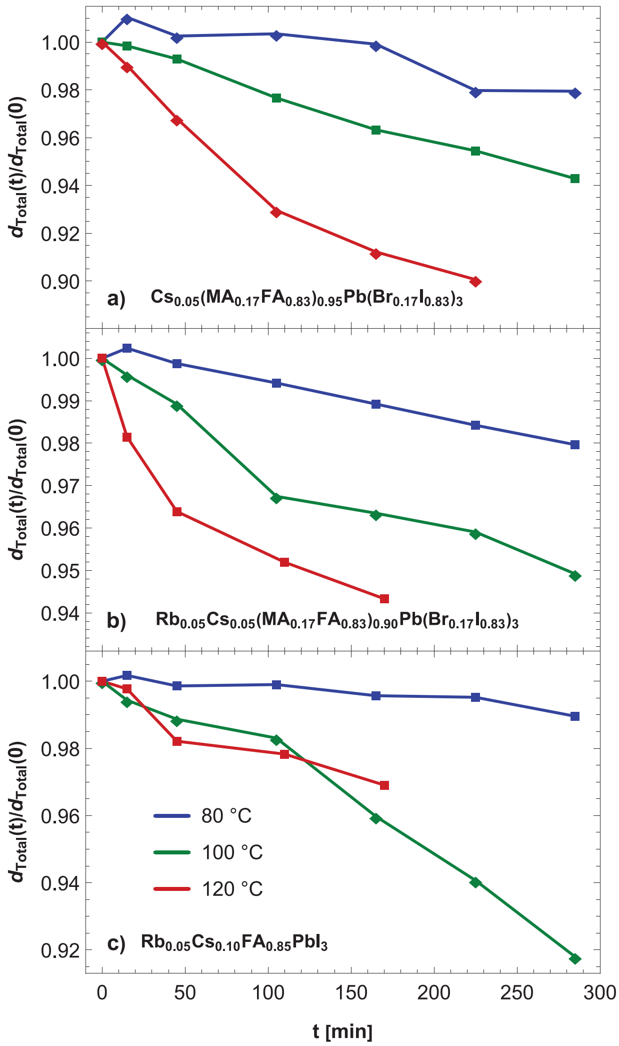

Figure 7. Relative variation in total fitted film thickness in the MIR region during thermally induced degradation for all considered perovskite compositions.

In accordance with the previous point, the relative changes in the fitted total thickness, that is, the roughness layer thickness added to the homogeneous film thickness, for the MIR region are shown in **Figure 7**. A comparison between the total thickness values from the MIR and DUV-NIR regions can be observed in Figure S7, Supporting Information. The differences between both spectral regions are attributed to the difficulty in assessing surface roughness in the DUV-NIR region, as well as differences in spot size and/or alignment between the two ellipsometers. Typical error margins for the total thickness are ±0.2–0.4%, according to a fit sensitivity analysis by the SpectraRay/4 software. Indeed, all films become thinner over time, with the MA-containing perovskites losing thickness roughly in tandem with the depletion of MA (Figure 5), and later FA (Figure 6 a,b). Similarly, the MA-free perovskite shows a rate of thickness loss roughly matching that of the loss of FA (Figure 6c).

A prominent concern is the rate at which MA and FA are depleted at temperatures of 100 °C and above, with substantial effects already after 30–60 min. Given that most standard solution processing recipes require annealing at similar temperatures and durations[1–10,17,20,23,27,34–37,42] (including the ones used in this work), concerns regarding the actual stoichiometry of pristine perovskite films can arise. Indeed, the data presented here suggests that, depending on annealing time, it is likely that some of the organic cations will have been lost during fabrication, leading to final film stoichiometries that differ significantly from the perovskite stock solutions.

3.3. Degradation Effects in the DUV to NIR Regions

In the DUV to NIR regions, all of the samples show relatively little change in the lower photon energy region, up to approximately 2 eV. At higher energies, however, the (n, k) spectra show considerable distortions, as can be seen in **Figure 8** for 100 °C. These consist mainly of higher absorption at energies of 4–6 eV, which becomes more pronounced with increasing degradation times. This effect is known and is attributed mainly to

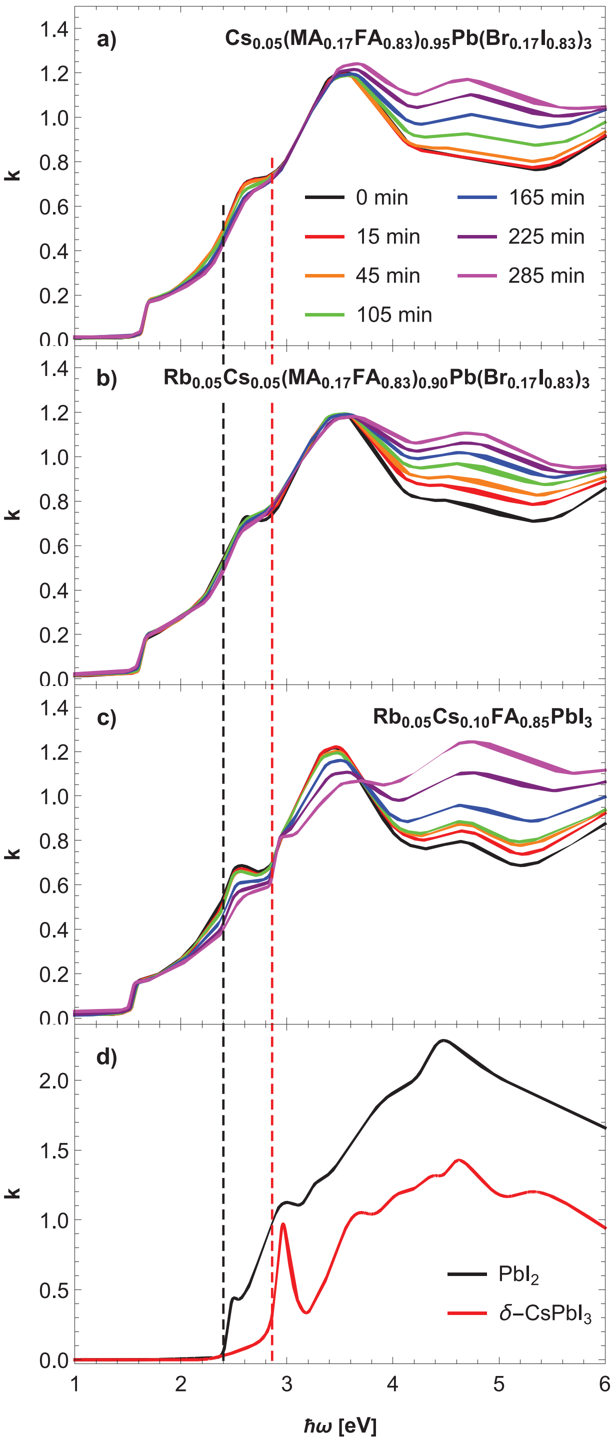

Figure 8. Extinction coefficients k for all considered perovskite compositions during thermally-induced degradation at 100 °C (a–c), as well as for pure PbI_2 and δ-$CsPbI_3$ (d).

the formation of PbI_2 within the films as the organic cations are lost,[17–22] and is further confirmed by the appearance of kinks around 2.4 eV in the k spectra, that is, at the absorption onset of PbI_2.[7,17] As noted previously, the baseline refractive index shows little change, as seen in Figure S6, Supporting Information. This suggests that structural effects on the base perovskite, such as changes in density, do not play an important role in these distortions.

A similar effect is observed in the MA-free perovskite, with another kink appearing at around 2.85 eV (Figure 8c). This coincides with the onset of a strong absorption peak in "yellow phase" non-perovskite δ-$CsPbI_3$,[27,43] suggesting the formation of this phase in addition to PbI_2 as the films degrade. For comparison purposes, the k spectra for PbI_2 and δ-$CsPbI_3$ are shown in Figure 8d. The optical data for these materials were obtained from ellipsometry measurements on evaporated films on fused silica substrates and are very similar to literature values.[7,27] The complete (n, k) datasets obtained for PbI_2 and δ-$CsPbI_3$ are shown in Figure S8, Supporting Information.

As the optical properties of PbI_2 and δ-$CsPbI_3$ are known, the concentration of these phases within the partially degraded perovskites can be estimated from the perovskite (n, k) spectra.[17] To accomplish this, the perovskite film was modeled as a ternary Bruggemann effective medium, composed of the base perovskite with PbI_2 and δ-$CsPbI_3$ inclusions. For these calculations, a custom script was written in Wolfram Mathematica. As the (n, k) spectra for all the considered phases are known, the inclusion volume fractions of these phases then serve as the only free parameters used to fit the measured (n, k) spectra of each of the partially degraded perovskites. For such a model to work, the same conditions as for traditional EMAs must be met, that is, these inclusions should be much smaller than the probing wavelength so as not to scatter light, but not so small as to not be distinguishable as separate phases.[24,28] Additionally, existing amounts of these phases prior to thermal degradation cannot be accounted for, as they would form part of the undegraded perovskite (n, k) spectra.

An example of this analysis for the degradation of $Rb_{0.05}Cs_{0.10}FA_{0.85}PbI_3$ at 100 °C is shown in **Figure 9**, where the k spectrum of the partially degraded perovskite is shown alongside that of the fitted EMA, for each time step of the annealing series. The EMA fits for the full (n, k) spectra for all samples are shown in Figures S9– S11, Supporting Information. It can be observed that the fitted EMAs describe the degraded perovskite well, but start to deviate for the two most degraded data sets. At this point, it is conceivable that the sizes of the PbI_2 and δ-$CsPbI_3$ inclusions become large enough that the EMA starts to break down. This may also be due to distortions in the higher energy regions of the (n, k) spectra due to increased grain size and therefore surface roughness, as seen in Figures S2– S4, Supporting Information. The PbI_2 volume fractions calculated using this method for all considered samples and temperatures are shown in **Figure 10**. The volume fractions for δ-$CsPbI_3$ are shown in **Figure 11** only for the MA-free $Rb_{0.05}Cs_{0.10}FA_{0.85}PbI_3$ composition at 80 and 100 °C, as they were the only data sets that showed a significant presence of this phase. For both Figures 10 and 11, error bars represent 95% confidence intervals calculated from constant error contours using bootstrap sampling.[44]

Overall, the formation of PbI_2 occurs at rates roughly corresponding to the loss of the organic cations observed in Figures 5 and 6, as well as to the reduction in total film thickness observed in Figure 7. This is consistent with the formation of PbI_2 as a stable by-product in the films as the perovskites

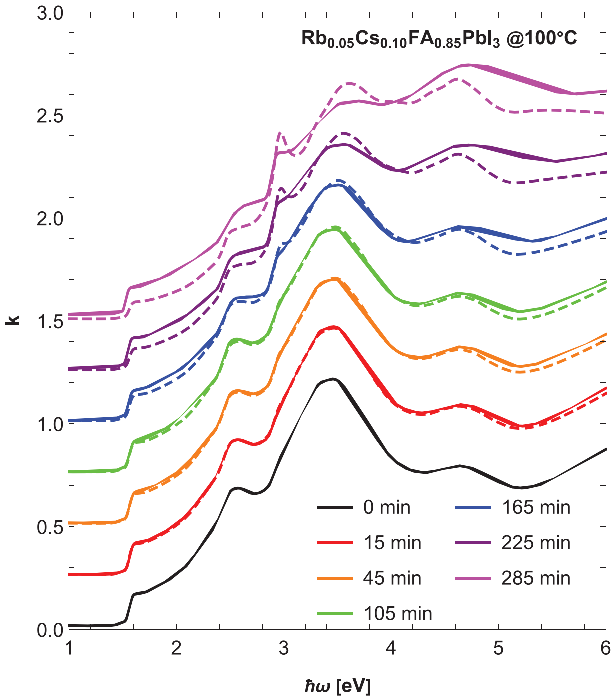

Figure 9. Bruggemann EMA fits on the extinction coefficient *k* spectra for $Rb_{0.05}Cs_{0.10}FA_{0.85}PbI_3$ at various stages of thermally induced degradation at 100 °C. The EMA is formed from the (*n*, *k*) spectra of the undegraded base perovskite and PbI_2, for varying volume fractions of the latter, as shown in 10. Solid lines correspond to the partially degraded perovskite, and dashed lines to the fitted EMA.

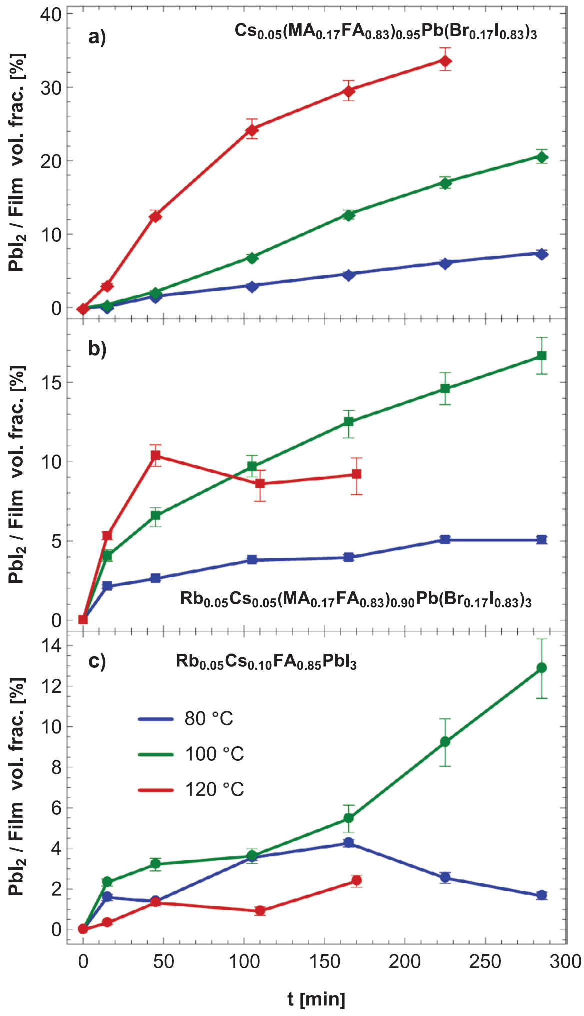

Figure 10. PbI_2-to-film volume fraction, as obtained from effective medium modeling for the considered perovskite compositions (a–c).

degrade, and is in agreement with the known decomposition pathways for MA-[17,18,20–22] and FA[19]-based perovskites. It can be observed that, for the same temperatures, the $Rb_{0.05}Cs_{0.05}(MA_{0.17}FA_{0.83})_{0.90}Pb(Br_{0.17}I_{0.83})_3$ perovskite composition forms PbI_2 at lower densities than the triple cation $Cs_{0.05}(MA_{0.17}FA_{0.83})_{0.95}Pb(Br_{0.17}I_{0.83})_3$ composition, suggesting an overall higher thermal stability of the former.

The formation of δ-$CsPbI_3$ within the MA-free $Rb_{0.05}Cs_{0.10}FA_{0.85}PbI_3$ perovskite also gives insight into its unusual behavior upon annealing, that is, the noticeably faster degradation at 100 °C than at 120 °C, and more pronounced PbI_2 formation at both 80 and 100 °C than at 120 °C (Figure 10c). This is attributed to a phase instability in this composition, similar to the behaviors of $FAPbI_3$ and $CsPbI_3$. Both of these compositions exhibit "black" perovskite phases that are metastable at room temperature and can readily transition into non-perovskite "yellow" δ-phases. The "black" phases are only truly stable at considerably higher temperatures.[27,43,45,46] It is then likely the case that, at 120 °C, the MA-free perovskite is closer to its minimum stable temperature than at 80 or 100 °C. In fact, at 120 °C, it is more stable than any of the other considered perovskite compositions, according to Figures 7 and 10.

To verify the validity of the EMA analysis for PbI_2 and δ-$CsPbI_3$, XRD measurements for samples of the MA-free perovskite as grown (undegraded) and after degradation at 100 and 120 °C are shown in **Figure 12**. The presence of PbI_2 in the undegraded sample is attributed to partial degradation during fabrication, and during the XRD measurement itself due to prolonged exposure to X-ray radiation and ambient air. While it is difficult to make quantitative observations, it can be seen that the known peaks for PbI_2 are larger in relation to those

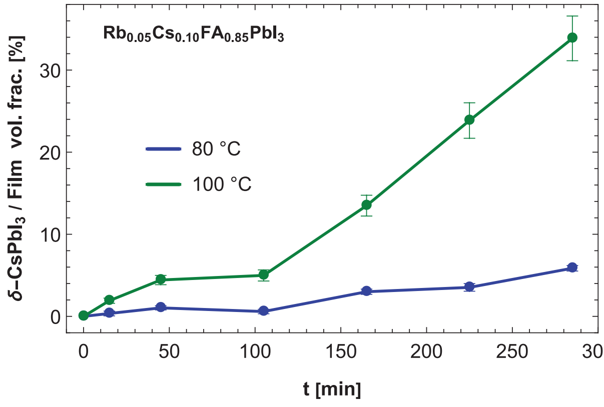

Figure 11. δ-$CsPbI_3$-to-film volume fraction, as obtained from effective medium modeling for the methylammonium-free $Rb_{0.05}Cs_{0.10}FA_{0.85}PbI_3$ perovskite composition.

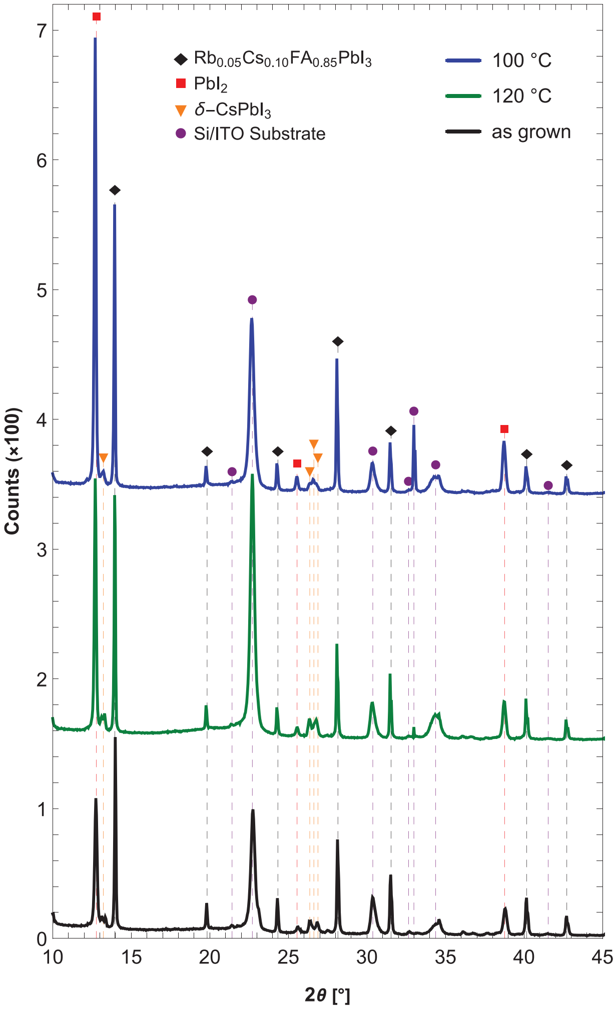

Figure 12. XRD measurements for the methylammonium-free $Rb_{0.05}Cs_{0.10}FA_{0.85}PbI_3$ perovskite composition: as grown, after 285 min anneal at 100 °C, and after 170 min anneal at 120 °C.

of the base perovskite[10] for the sample after degradation at 100 °C than for the one after degradation at 120 °C, suggesting higher concentrations of these phases. At the same time, both degraded samples show larger PbI_2 peaks in relation to the base perovskite than the undegraded sample. These results are consistent with the trends observed in Figures 10 and 11. The concentration of δ-$CsPbI_3$ is more difficult to qualitatively gauge from its known diffraction peaks,[27,43] as they are very small. However, its presence is much more evident in relation to the undegraded samples from the *k* spectra in Figure 8 and Figure S11, Supporting Information.

4. Summary

Various device-relevant multi-cation hybrid perovskites were characterized using spectroscopic ellipsometry in a very wide spectral range, covering wavelengths from 200 nm to 25 µm. This allowed a fully quantitative and precise tracking of changes in the perovskites' (*n*, *k*) spectra, as well as film thickness and surface roughness, during thermally induced degradation at temperatures of 80, 100, and 120 °C. The studied perovskites included a triple cation composition ($Cs_{0.05}(MA_{0.17}FA_{0.83})_{0.95}Pb(Br_{0.17}I_{0.83})_3$), a Rb-containing variant ($Rb_{0.05}Cs_{0.05}(MA_{0.17}FA_{0.83})_{0.90}Pb(Br_{0.17}I_{0.83})_3$), as well as a methylammonium-free one ($Rb_{0.05}Cs_{0.10}FA_{0.85}PbI_3$). It was possible to quantify changes in the concentration of methylammonium and formamidinium cations over time, and demonstrate that PbI_2 and non-perovskite δ-$CsPbI_3$ phase inclusions are simultaneously formed within the films as degradation by-products. The entire analysis was performed purely on quick and non-destructive optical measurements.

Methylammonium was completely depleted from the triple cation perovskite and it's Rb-containing variant within 285 min at temperatures above 100 °C. The concentration of formamidinium in the same samples simultaneously increased due the rapid change in stoichiometry, and then began decreasing after the MA was depleted. This was accompanied by the formation of PbI_2 at rates roughly matching the depletion of the organic cations. Overall, the triple cation composition was significantly less stable than its Rb-containing variant at 120 °C, with greater rates of PbI_2 formation and organic cation depletion for the same degradation time steps. At lower temperatures, the discrepancy was less pronounced. The methylammonium-free composition showed a markedly different behavior, with only a decrease in formamidinium concentration at all temperatures. Unlike the methylammonium-containing samples, it was highly stable at 120 °C but degraded much more rapidly at lower temperatures. This was attributed to a phase instability similar to that observed in $FAPbI_3$ and $CsPbI_3$,[27,43,45,46] leading to the observed formation of non-perovskite δ-$CsPbI_3$ within films with this composition, in addition to PbI_2. In all cases, the significant changes in film composition during annealing at temperatures around 100 °C, which are often done during film fabrication,[1–10,17,20,23,27,34–37,42] raise concerns over the assumed initial stoichiometries of the films.

Supporting Information

Supporting Information is available from the Wiley Online Library or from the author.

Acknowledgements

This work was partially funded by the German Federal Ministry for Education and Research (BMBF, grant 03SF0540), the HyperCells Graduate School, and the Helmholtz Association within the HySPRINT Innovation lab project and TAPAS project. Additional funding was provided by the Peruvian National Fund for Scientific and Technological Development (FONDECYT, grant 179-2020-FONDECYT), the German Academic Exchange Service (DAAD) in conjunction with FONDECYT (grants 57508544 and 423-2019-FONDECYT, respectively), as well as by the PUCP vicechancellorship for research (VRI, project CAP-2019-3-0041/702). The authors gratefully acknowledge Bor Li and Hampus Näsström for their aid in sample manufacturing, Marcel Roß for the XRD measurements and sample preparation, Ganna Chistiakova for additional ellipsometry measurements, Anna Morales for the ITO deposition, as well as Carola Ferber, Monika Gabernig, and Hagen Heinz in the HySPRINT lab. A.T. gratefully acknowledges the

Peruvian National Council for Science, Technology and Technological Innovation (CONCYTEC) for a Ph.D. scholarship under grant no. 236-2015-FONDECYT.

Open access funding enabled and organized by Projekt DEAL.

Conflict of Interest

The authors declare no conflict of interest.

Data Availability Statement

Research data are not shared.

Keywords

bond density, effective medium approximation, ellipsometry, hybrid perovskites

Received: July 28, 2021
Revised: October 23, 2021

[1] J. A. Guerra, A. Tejada, L. Korte, L. Kegelmann, J. A. Töfflinger, S. Albrecht, B. Rech, R. Weingärtner, *J. Appl. Phys.* **2017**, *121*, 173104.
[2] E. Köhnen, M. Jošt, A. Morales Vilches, P. Tockhorn, A. Al-Ashouri, B. Macco, L. Kegelmann, L. Korte, B. Rech, R. Schlatmann, B. Stannowski, S. Albrecht, *Sustainable Energy Fuels* **2019**, *3*, 1995.
[3] M. Saliba, T. Matsui, J. Y. Seo, K. Domanski, J. P. Correa-Baena, M. K. Nazeeruddin, S. M. Zakeeruddin, W. Tress, A. Abate, A. Hagfeldt, M. Grätzel, *Energy Environ. Sci.* **2016**, *9*, 1989.
[4] M. Saliba, T. Matsui, K. Domanski, J.-Y. Seo, A. Ummadisingu, S. M. Zakeeruddin, J.-P. Correa-Baena, W. R. Tress, A. Abate, A. Hagfeldt, M. Gratzel, *Science* **2016**, *354*, 206.
[5] M. Saliba, J. P. Correa-Baena, C. M. Wolff, M. Stolterfoht, N. Phung, S. Albrecht, D. Neher, A. Abate, *Chem. Mater.* **2018**, *30*, 4193.
[6] G. Schuck, D. M. Többens, M. Koch-Müller, I. Efthimiopoulos, S. Schorr, *J. Phys. Chem. C* **2018**, *122*, 5227.
[7] M. Shirayama, H. Kadowaki, T. Miyadera, T. Sugita, M. Tamakoshi, M. Kato, T. Fujiseki, D. Murata, S. Hara, T. N. Murakami, S. Fujimoto, M. Chikamatsu, H. Fujiwara, *Phys. Rev. Appl.* **2016**, *5*, 014012.
[8] A. Tejada, S. Braunger, L. Korte, S. Albrecht, B. Rech, J. A. Guerra, *J. Appl. Phys.* **2018**, *123*, 175302.
[9] S. H. Turren-Cruz, M. Saliba, M. T. Mayer, H. Juárez-Santiesteban, X. Mathew, L. Nienhaus, W. Tress, M. P. Erodici, M. J. Sher, M. G. Bawendi, M. Grätzel, A. Abate, A. Hagfeldt, J. P. Correa-Baena, *Energy Environ. Sci.* **2018**, *11*, 78.
[10] S. H. Turren-Cruz, A. Hagfeldt, M. Saliba, *Science* **2018**, *362*, 449.
[11] A. Al-Ashouri, E. Köhnen, B. Li, A. Magomedov, H. Hempel, P. Caprioglio, J. A. Márquez, A. B. M. Vilches, E. Kasparavicius, J. A. Smith, N. Phung, D. Menzel, M. Grischek, L. Kegelmann, D. Skroblin, C. Gollwitzer, T. Malinauskas, M. Jošt, G. Matič, B. Rech, R. Schlatmann, M. Topič, L. Korte, A. Abate, B. Stannowski, D. Neher, M. Stolterfoht, T. Unold, V. Getautis, S. Albrecht, *Science* **2020**, *370*, 1300.
[12] J. Jeong, M. Kim, J. Seo, H. Lu, P. Ahlawat, A. Mishra, Y. Yang, M. A. Hope, F. T. Eickemeyer, M. Kim, Y. J. Yoon, I. W. Choi, B. P. Darwich, S. J. Choi, Y. Jo, J. H. Lee, B. Walker, S. M. Zakeeruddin, L. Emsley, U. Rothlisberger, A. Hagfeldt, D. S. Kim, M. Grätzel, J. Y. Kim, *Nature* **2021**, *592*, 381.
[13] M. De Bastiani, E. Van Kerschaver, Q. Jeangros, A. Ur Rehman, E. Aydin, F. H. Isikgor, A. J. Mirabelli, M. Babics, J. Liu, S. Zhumagali, E. Ugur, G. T. Harrison, T. G. Allen, B. Chen, Y. Hou, S. Shikin, E. H. Sargent, C. Ballif, M. Salvador, S. De Wolf, *ACS Energy Lett.* **2021**, *6*, 2944.
[14] F. Fu, S. Pisoni, Q. Jeangros, J. Sastre-Pellicer, M. Kawecki, A. Paracchino, T. Moser, J. Werner, C. Andres, L. Duchêne, P. Fiala, M. Rawlence, S. Nicolay, C. Ballif, A. N. Tiwari, S. Buecheler, *Energy Environ. Sci.* **2019**, *12*, 3074.
[15] M. V. Khenkin, E. A. Katz, A. Abate, G. Bardizza, J. J. Berry, C. Brabec, F. Brunetti, V. Bulović, Q. Burlingame, A. Di Carlo, R. Cheacharoen, Y. B. Cheng, A. Colsmann, S. Cros, K. Domanski, M. Dusza, C. J. Fell, S. R. Forrest, Y. Galagan, D. Di Girolamo, M. Grätzel, A. Hagfeldt, E. von Hauff, H. Hoppe, J. Kettle, H. Köbler, M. S. Leite, S. F. Liu, Y. L. Loo, J. M. Luther, et al., *Nat. Energy* **2020**, *5*, 35.
[16] NREL, https://www.nrel.gov/pv/cell-efficiency.html (accessed: July 2021).
[17] X. Wang, J. Gong, X. Shan, M. Zhang, Z. Xu, R. Dai, Z. Wang, S. Wang, X. Fang, Z. Zhang, *J. Phys. Chem. C* **2019**, *123*, 1362.
[18] E. J. Juarez-Perez, L. K. Ono, M. Maeda, Y. Jiang, Z. Hawash, Y. Qi, *J. Mater. Chem. A* **2018**, *6*, 9604.
[19] E. J. Juarez-Perez, L. K. Ono, Y. Qi, *J. Mater. Chem. A* **2019**, *7*, 16912.
[20] G. Abdelmageed, L. Jewell, K. Hellier, L. Seymour, B. Luo, F. Bridges, J. Z. Zhang, S. Carter, *Appl. Phys. Lett.* **2016**, *109*, 23.
[21] G. Murugadoss, S. Tanaka, G. Mizuta, S. Kanaya, H. Nishino, T. Umeyama, H. Imahori, S. Ito, *Jpn. J. Appl. Phys.* **2015**, *54*, 8.
[22] N. Phung, A. Abate, *Small* **2018**, *14*, 1802573.
[23] P. Löper, M. Stuckelberger, B. Niesen, J. Werner, M. Filipič, S.-J. Moon, J.-H. Yum, M. Topič, S. De Wolf, C. Ballif, *J. Phys. Chem. Lett.* **2015**, *6*, 66.
[24] H. Fujiwara, in *Spectroscopic Ellipsometry for Photovoltaics*, (Eds: H. Fujiwara, R. W. Collins), Vol. *1*, Springer, Cham **2018**, pp. 155–172.
[25] S. Fujimoto, T. Fujiseki, M. Tamakoshi, A. Nakane, T. Miyadera, T. Sugita, T. N. Murakami, M. Chikamatsu, H. Fujiwara, in *Spectroscopic Ellipsometry for Photovoltaics*, (Eds: H. Fujiwara, R. W. Collins) Vol. *2*, Springer, Cham, Switzerland **2018**, pp. 471–493.
[26] M. I. Alonso, B. Charles, A. Francisco-López, M. Garriga, M. T. Weller, A. R. Goñi, *J. Vac. Sci. Technol. B* **2019**, *37*, 062901.
[27] M. Yuan, L. Yuan, Z. Hu, Z. Yu, H. Li, E. M. Barea, J. Bisquert, X. Meng, *J. Phys. Chem. C* **2020**, *124*, 8008.
[28] H. Fujiwara, *Spectroscopic Ellipsometry: Principles and Applications*, Wiley, Chichester, UK **2007**.
[29] N. Rajamanickam, S. Kumari, V. K. Vendra, B. W. Lavery, J. Spurgeon, T. Druffel, M. K. Sunkara, *Nanotechnology* **2016**, *27*, 235404.
[30] W. Kern, D. A. Puotinen, *RCA Rev.* **1970**, *31*, 187.
[31] A. Al-Ashouri, A. Magomedov, M. Roß, M. Jošt, M. Talaikis, G. Chistiakova, T. Bertram, J. A. Márquez, E. Köhnen, E. Kasparavičius, S. Levcenco, L. Gil-Escrig, C. J. Hages, R. Schlatmann, B. Rech, T. Malinauskas, T. Unold, C. A. Kaufmann, L. Korte, G. Niaura, V. Getautis, S. Albrecht, *Energy Environ. Sci.* **2019**, *12*, 3356.
[32] R. A. Synowicki, *Thin Solid Films* **1998**, *313-314*, 394.
[33] R. Santbergen, R. Mishima, T. Meguro, M. Hino, H. Uzu, J. Blanker, K. Yamamoto, M. Zeman, *Opt. Express* **2016**, *24*, A1288.
[34] P. Wang, J. Guan, D. T. Galeschuk, Y. Yao, C. F. He, S. Jiang, S. Zhang, Y. Liu, M. Jin, C. Jin, Y. Song, *J. Phys. Chem. Lett.* **2017**, *8*, 2119.

[35] K. Kawamura, R. Ishikawa, Y. Wasai, N. Nabatova-Gabain, S.-j. Kurosu, T. Ukai, M. Tokuda, Y. Fujii, T. Hanajiri, K. Ueno, H. Shirai, *J. Vac. Sci. Technol. B* **2019**, *37*, 062401.

[36] Z. Zhou, S. Pang, F. Ji, B. Zhang, G. Cui, *Chem. Commun.* **2016**, *52*, 3828.

[37] T. Glaser, C. Müller, M. Sendner, C. Krekeler, O. E. Semonin, T. D. Hull, O. Yaffe, J. S. Owen, W. Kowalsky, A. Pucci, R. Lovrinčić, *J. Phys. Chem. Lett.* **2015**, *6*, 2913.

[38] H. Kuzmany, *Solid-State Spectroscopy*, Springer-Verlag, Berlin Heidelberg, Germany **2009**.

[39] M. Sendner, J. Trollmann, A. Pucci, *Org. Electron.* **2014**, *15*, 2959.

[40] S. Gallis, V. Nikas, E. Eisenbraun, M. Huang, A. E. Kaloyeros, *J. Mater. Res.* **2009**, *24*, 2561.

[41] H. Takahashi, H. Kataoka, H. Nagata, *J. Mater. Res.* **1997**, *12*, 1722.

[42] A. Latini, G. Gigli, A. Ciccioli, *Sustainable Energy Fuels* **2017**, *1*, 1351.

[43] G. E. Eperon, G. M. Paternò, R. J. Sutton, A. Zampetti, A. A. Haghighirad, F. Cacialli, H. J. Snaith, *J. Mater. Chem. A* **2015**, *3*, 19688.

[44] W. H. Press, S. A. Teukolsky, W. T. Vetterling, B. P. Flannery, *Numerical Recipes: The Art of Scientific Computing*, 3rd ed., Cambridge University Press, New York **2007**.

[45] V. L. Pool, B. Dou, D. G. Van Campen, T. R. Klein-Stockert, F. S. Barnes, S. E. Shaheen, M. I. Ahmad, M. F. Van Hest, M. F. Toney, *Nat. Commun.* **2017**, *8*, 14075.

[46] T. Chen, B. J. Foley, C. Park, C. M. Brown, L. W. Harriger, J. Lee, J. Ruff, M. Yoon, J. J. Choi, S. H. Lee, *Sci. Adv.* **2016**, *2*, e1601650.